J. Fluid Mech. (1966), *vol.* 26, *part* 3, *pp.* 577–598
Printed in Great Britain

Numerical solutions of the steady-state vorticity equation in rectangular basins

By JOHN A. T. BYE
University of California, San Diego, Scripps Institution of Oceanography
La Jolla, California

(Received 17 June 1965 and in revised form 26 March 1966)

The Navier–Stokes vorticity equation is solved numerically for the circulation induced in a vertical plane, by a constant stress acting on a liquid, enclosed in a basin of uniform depth and vertical sides.

Solutions of the linearized vorticity equation are obtained for all Reynolds numbers ($\tau_s D^2/4\rho\nu^2$ where τ_s is the surface stress, ρ is the density, ν is the kinematic viscosity, and D is the depth of the liquid) and solutions of the complete vorticity equation for Reynolds numbers 0–400.

The notable feature of the solutions is the totally different end circulations. At the upwind end the flow becomes very slack, and the vorticity equation has a boundary-layer limit, while at the downwind end a damped wave occurs and the equation has an inviscid limit.

At Reynolds numbers between 400 and 600, the streamlines at the downwind end lead to a condition of hydrodynamic instability, in approximate agreement with some experimental observations by G. H. Keulegan.

1. Introduction

This paper is a study of the solution of the equations of fluid motion in an enclosed basin. The flow considered is that induced by a constant surface stress acting along the surface of a liquid contained in a basin of uniform depth and vertical sides. We solve numerically the Navier–Stokes equation for circulation in a vertical plane in the direction of the applied stress.

The problem appears to have been studied theoretically before by Hidaka (1939). He, without the aid of an electronic computer, was not able to obtain any extensive results. In the present work, solutions of the vorticity equation are obtained for the steady-state flow up to a high enough Reynolds number for the streamlines to indicate a condition of hydrodynamic instability. The Reynolds number at which this occurs has been observed experimentally by Keulegan (1951) in a laboratory investigation of wind-tides at low Reynolds numbers. His findings are in approximate agreement with our result. The essential feature of the solutions is that, as the Reynolds number increases, the end circulations extend progressively further from the walls and become totally different from one another.

Basically, an excess of energy is supplied to the liquid through the shearing

stress at the upwind† end, and transferred to the downwind end, where it is radiated away in the form of a damped wave, which is eventually of sufficient amplitude to lead to a condition of hydrodynamic instability. In brief, upwind the vorticity equation has a boundary-layer limit, and downwind an inviscid limit.

2. The Problem

We will consider the circulation induced by a constant and uniform surface stress (τ_s), acting in the plane (x, z) of a liquid enclosed in the basin shown in figure 1.

It will be assumed that the sides are far enough away from the plane (x, z) for their influence to be negligible, and also that the depth of the liquid is sufficiently small for Coriolis forces to be unimportant compared with inertial and

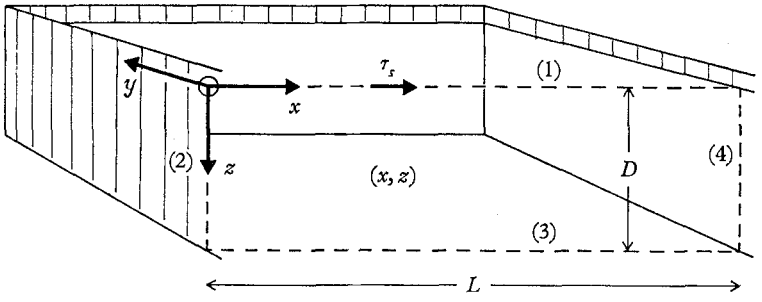

FIGURE 1. The rectangular basin.

viscous forces. The differential operators in the y-direction ($\partial/\partial y$), therefore can be set identically zero, and the analysis becomes strictly two-dimensional.

The equations of motion are as follows:

$$u\frac{\partial u}{\partial x}+w\frac{\partial u}{\partial z}=-\frac{1}{\rho}\frac{\partial p}{\partial x}+\nu\nabla^2 u; \tag{1}$$

$$u\frac{\partial w}{\partial x}+w\frac{\partial w}{\partial z}=-\frac{1}{\rho}\frac{\partial p}{\partial z}+\nu\nabla^2 w+g; \tag{2}$$

where $\nabla^2=(\partial^2/\partial x^2)+(\partial^2/\partial z^2)$, u is the velocity component in the x-direction, w is the velocity component in the z-direction (z measured vertically downwards), p is the pressure, g is the acceleration of gravity, ρ is the density of the liquid, and ν is the dynamic viscosity of the liquid.

We now make use of the two-dimensional continuity equation to define the velocity components in terms of the streamfunction (ψ),

$$u=-\partial\psi/\partial z, \quad w=\partial\psi/\partial x \tag{3}$$

† The term 'upwind' more precisely should be 'upstress', but upwind and downwind will be used throughout the paper because of their familiarity.

and by differentiating equation (1), w.r.t. z, and equation (2) w.r.t. x, eliminate the pressure derivatives, and obtain the two-dimensional vorticity equation,

$$\left(-\frac{\partial\psi}{\partial z}\frac{\partial}{\partial x}+\frac{\partial\psi}{\partial x}\frac{\partial}{\partial z}\right)\nabla^2\psi=\nu\nabla^4\psi, \tag{4}$$

where

$$\nabla^4=\frac{\partial^4}{\partial x^4}+2\frac{\partial^4}{\partial x^2\partial z^2}+\frac{\partial^4}{\partial z^4}.$$

Equation (4) is solved numerically below with the boundary conditions of constant applied surface stress, and no-slip on the sides and bottom; i.e. on the top surface of the liquid (1 in figure 1),

$$\psi=0, \quad \tau_s=\rho\nu\frac{\partial^2\psi}{\partial z^2}\Big)_{z=0},$$

on the bottom (3 in figure 1),

$$\psi=0, \quad u=-\frac{\partial\psi}{\partial z}\Big)_{z=D}=0,$$

and on the sides, respectively (2 and 4 in figure 1),

$$\psi=0, \quad w=\frac{\partial\psi}{\partial x}\Big)_{x=0}=0,$$

and

$$\psi=0, \quad w=\frac{\partial\psi}{\partial x}\Big)_{x=L}=0.$$

Here, the origin (0) of the co-ordinate system is on the surface of the liquid at the upwind wall of the basin, D is the depth of the liquid, and L is the length of the basin.

The first of these boundary conditions assumes that we neglect the effect of any free displacement of the surface due to the motion of the liquid. Before proceeding to the solution let us examine this assumption by deriving a general expression for the surface elevation (ξ) from the equations of motion. Integrating equations (1) and (2) w.r.t. z, and applying the continuity equation, we have, respectively

$$\int_{-\xi}^{D}\frac{\partial u^2}{\partial x}dz=\int_{-\xi}^{D}\left(-\frac{1}{\rho}\frac{\partial p}{\partial x}+\nu\nabla^2 u\right)dz, \tag{5a}$$

$$w^2=-\frac{1}{\rho}(P-P_a)+\int_{-\xi}^{D}\nu\nabla^2 w\,dz+g(z+\xi), \tag{5b}$$

where P_a is the atmospheric pressure.

Thus, substituting equation (5b) into equation (5a), assuming $\partial P_a/\partial x=0$, and rearranging, we obtain,

$$\frac{\partial\xi}{\partial x}=\frac{\tau_s}{\rho g(D+\xi)}\left[1-\frac{\tau_b}{\tau_s}-\frac{\rho}{\tau_s}\left\{\nu\int_{-\xi}^{D}\int_{-\xi}^{z}\frac{\partial}{\partial x}\nabla^2 w\,dz\,dz+\int_{-\xi}^{D}\frac{\partial}{\partial x}(u^2-w^2)\,dz\right\}\right], \tag{6}$$

where τ_b is the stress on the bottom of the basin. The surface slope $\partial\xi/\partial x$ therefore contains terms arising both from the viscous and the inertial terms of the equations of motion. It is strictly negligible only for infinite g. However, provided that $\tau_s/\rho g(D+\xi)$ is small, computed surface slopes $\partial\xi/\partial x$ in all our solutions are also small.

Let us now non-dimensionalize equation (4), and the boundary conditions by defining,

$$X = x/D, \quad Z = z/D, \quad \phi = \psi\rho\nu/\tau_s D^2.$$

Then, we obtain

$$\frac{\tau_s D^2}{\rho\nu^2}\left(-\frac{\partial\phi}{\partial Z}\frac{\partial}{\partial X}+\frac{\partial\phi}{\partial X}\frac{\partial}{\partial Z}\right)\nabla^2\phi = \nabla^4\phi \tag{7}$$

with boundary conditions analogous to the dimensional equation, but with a unit non-dimensional surface stres

$$\left.\frac{\partial^2\phi}{\partial Z^2}\right)_{Z=0} = 1.$$

Solutions of equation (7) are derived below for various values of the parameter

$$\tau_s D^2/(\rho\nu^2). \tag{8}$$

3. The limiting forms of solution

(*a*) *The mid-basin solution*

At an infinite distance from the end walls of the basin, the X-derivatives in equation (7) vanish, and at all finite values of $(\tau_s D^2/\rho\nu^2)$, we obtain the one-dimensional vorticity equation

$$\partial^4\phi/\partial Z^4 = 0. \tag{9}$$

The solution of equation (9) is the mid-basin solution (ϕ_0). Integrating, and applying the boundary conditions, we obtain

$$\phi_0 = -Z(Z-1)^2. \tag{10}$$

The associated stress profile

$$\tau_0 = \tau_s(1-\tfrac{3}{2}Z) \tag{11}$$

is linear, and substituting into the one-dimensional form of equation (6), we derive the mid-basin surface slope,

$$\frac{\partial\xi_0}{\partial x} = \frac{\tau_s}{\rho g(D+\xi)}\left(1-\frac{\tau_b}{\tau_s}\right) = \frac{\frac{3}{2}\tau_s}{\rho g(D+\xi)}. \tag{12}$$

The velocity profile,

$$U_0 = \{\tau_s D/(4\rho\nu)\}(3Z-1)(Z-1) \tag{13}$$

is parabolic (figure 2), and the mid-basin surface velocity,

$$U_s = \tau_s D/(4\rho\nu)$$

defines a Reynolds number (Re) for the solutions,

$$Re = \left(\frac{\tau_s D}{4\rho\nu}\right)\frac{D}{\nu}$$

in terms of the parameter (8).

(*b*) *The eigenequation asymptotic to the mid-basin solution*

Asymptotic to the mid-basin solution, i.e. at large distances from the end walls of the basin, we seek a solution, by expanding the streamfunction, ϕ, as a small perturbation on the mid-basin solution.

$$\phi = \phi_0 + \epsilon, \tag{14}$$

where $$\epsilon = Af(Z)\, e^{\lambda X}$$

and λ is a function of the Reynolds number (Re).

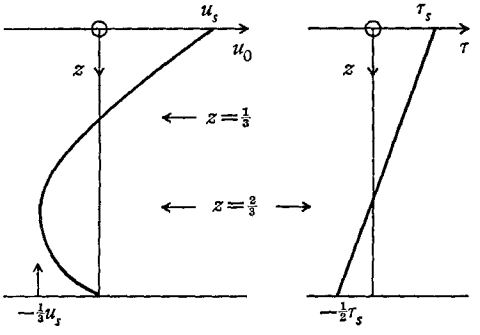

FIGURE 2. The mid-basin stress and velocity profiles.
$u_s = \tau_s D/4\rho\nu$.

Substituting equation (14) into the non-dimensional vorticity equation, and considering only terms of $O(\epsilon)$, we obtain

$$f^{\mathrm{iv}} + 2\lambda^2 f'' + \lambda^4 f = -4Re\,\lambda[\phi_0'\lambda^2 f + \phi_0' f'' - \phi_0''' f], \tag{15}$$

where the primes denote differentiation w.r.t. Z.

Equation (15), which is ordinary fourth order, is a linearized vorticity equation. As there are four homogeneous boundary conditions on $f(Z)$,

$$f(0) = 0, \quad f(1) = 0, \quad f''(0) = 0, \quad f'(1) = 0.$$

it is an eigenequation—the exponent λ, is an eigenvalue, and $f(Z)$ is the corresponding eigenfunction.

Let us consider the solution of equation (15), under the limiting processes of (i) $Re \to 0$, (ii) $Re \to \infty$.

(*c*) *The limiting solutions of the eigenequation*

(i) $Re \to 0$

As $Re \to 0$, equation (15) tends to

$$f^{\mathrm{iv}} + 2\lambda^2 f'' + \lambda^4 f = 0 \tag{16}$$

which is derived from the linearized form of the Navier–Stokes equations, namely the biharmonic equation,

$$\nabla^4\phi = 0.$$

A notable feature of equation (16) is that it is symmetrical in λ. Hence,

$$f(Z)\, e^{-\lambda X}$$

is also a solution, and ϕ is independent of the sign of the surface stress (τ_s). The solution of equation (16) has been obtained by methods recently developed by the author†, and is recorded in table 1.

			$F(Z)$				
	A	λ	$Z \to 0{\cdot}167$	0·333	0·5	0·667	0·833
From equation (16)	—	$\pm 3{\cdot}9$	0·66	1	0·94	0·58	0·17
Relaxation solution	0·13	$\pm 3{\cdot}7$	0·66	1	0·96	0·61	0·20

TABLE 1. The $Re = 0$ parameters

(ii) $Re \to \infty$

For $Re > 0$, equation (15) is not symmetrical in λ. Hence, ϕ depends on the sign of τ_s. In other words, we expect to find *two* types of solutions to the equation; one appropriate to flow upwind of the mid-basin flow, and the other to flow downwind.

Let us discover the limiting forms of these solutions as $Re \to \infty$. Consider first the physical processes which are involved. Energy is transferred from one end of the basin to the other by the mid-basin flow in three ways: by transport of kinetic energy, by transport of potential energy, and by working of pressure forces. There is no mass flow, and the liquid is in hydrostatic equilibrium, and so the rate of working of the pressure forces is equal and opposite to the flux of potential energy. The total energy is therefore given by the kinetic energy transfer, which clearly transports energy from the upwind to the downwind end of the basin. This implies that the upwind flow produces an excess of energy and that the surface shearing stress, which is the only means of supplying energy to the liquid must here play an essential part. On the other hand the downwind circulation must dissipate an excess of energy, and, if we assume that the Reynolds number is not so high that turbulent breakdown occurs, this excess energy is likely to be radiated away in the form of a damped wave.

Hence, in brief, we expect a boundary-layer limit to equation (15) to be appropriate upwind, and an inviscid limit downwind. As $Re \to \infty$, therefore, at the upwind end,

$$f^{\mathrm{iv}} = -4Re\,\lambda(\phi_0' f'' - \phi_0''' f) \tag{17}$$

and at the downwind end,

$$\phi_0'\lambda^2 f + \phi_0' f'' - \phi_0''' f = 0. \tag{18}$$

† The basis of the method of solution is described in Bye (1966). Equation (16), is of some mathematical interest, since it is not strictly an eigenequation, although at least one special solution exists (table 1).

Equation (17) is an exact linearization of the boundary-layer vorticity equation,

$$\frac{\partial^4\phi}{\partial Z^4} = 4Re\left(-\frac{\partial\phi}{\partial Z}\frac{\partial^3\phi}{\partial X\,\partial Z^2}+\frac{\partial\phi}{\partial X}\frac{\partial^3\phi}{\partial Z^3}\right)$$

and equation (18) is derived by formally letting $Re \to \infty$ in equation (15).

Finite-difference solutions of equations (17) and (18) have been obtained, using a programme of the Oxford University Laboratory, based on the method of inverse iteration, with mesh intervals, respectively, $h_Z = \frac{1}{19}$, and $h_Z = \frac{1}{24}$, $\frac{1}{12}\cdots\frac{1}{12}, \frac{1}{24}$.

			$F(Z)$				
	λ	θ	$Z \to 0{\cdot}167$	0·333	0·5	0·667	0·833
Upwind	$-40{\cdot}0/Re$	—	0·65	1	0·96	0·62	0·19
Downwind	$\pm 3{\cdot}72i$	1·70	0·22	0·67	1	0·79	0·48

TABLE 2. The $Re = \infty$ parameters

The fundamental eigenparameters are recorded in table 2, and the eigenfunctions are shown in figures 3 and 4.

We note that consistent with our physical argument:

(*a*) The negative $Re\,\lambda$ of equation (17) implies an upwind solution. Thus the limiting upwind perturbation as $Re \to \infty$, is exponential with a zero decay factor.

(*b*) the negative (λ^2) of equation (18) implies an oscillating flow with a wavelength,

$$\theta = 2\pi/|\lambda|.$$

Hence the limiting downwind perturbation as $Re \to \infty$, is an undamped oscillation. Harmonic eigenvalues of equation (17), with $Re\,\lambda$ negative, have also been obtained. However, as the full solution of the vorticity equation refers to the fundamental mode, they will not be discussed further (§ 4). No harmonic solutions with a negative λ^2 were obtained for equation (18).

(*d*) *The full solution of the eigenequation*

The approach to the limiting eigenvalues has been studied by the numerical solution of the complete eigenequation (15). We assumed a series of values for λ, and solved the equation as an eigenvalue problem in Re, using a Texas University Computer Programme entitled 'F4UTEXMATSUB'. Graphs were then drawn showing the variation of λ with Re.

The discrepancies between the eigenvalues of the limiting equations, and the eigenvalues of equation (15) in the limit $Re \to \infty$, are due to the cruder finite-difference networks ($h_Z = \frac{1}{6}, \frac{1}{3}, \frac{1}{3}, \frac{1}{6}$) used in the latter solution.

(i) *The upwind solution*

The approach to the limiting upwind eigenvalue is shown in figure 5.

As Re increases, $|\lambda|$ decreases, or, in physical terms since λ is real, the decay factor of the upwind perturbation tends to zero. In this manner, equation (15)

tends to the limiting equation (17). $|Re\,\lambda|$ increases rapidly with Re, and has already attained about 90 % of its limiting value at $Re = 50$.

Thus, the boundary-layer equation is a good approximation even at quite low Reynolds numbers.

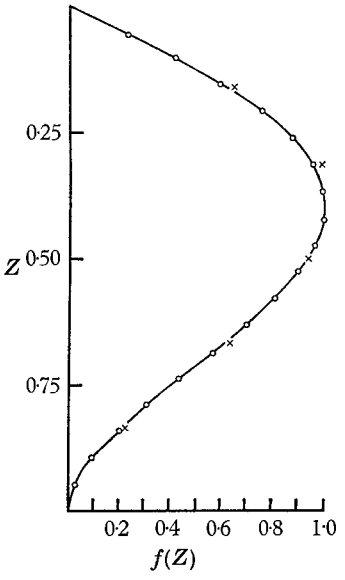

FIGURE 3. The limiting upwind eigenfunction. ○, Re = ∞; ×, third-order relaxation solution ($Re = 400$).

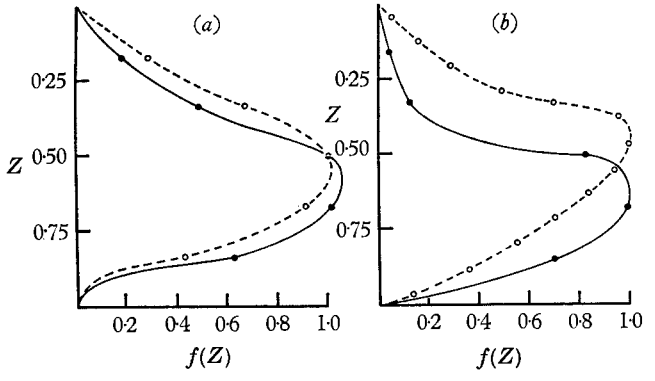

FIGURE 4. The downwind eigenfunctions. (*a*) ○, $Re = 40$; ●, $Re = 400$; (*b*) ○, $Re = \infty$; ●, $Re = \infty$ (special solution).

(ii) *The downwind solution*

In the downwind solution, λ is a complex number. Let us therefore define the complex eigenparameters thus:

$$\lambda = -\mu + 2\pi i/\theta, \quad h(Z) = g(Z) + ip(Z).$$

Then, rewriting equation (14) equivalently, we have

$$\begin{aligned}\phi &= \phi_0 + Ah(Z)\, e^{\lambda\zeta} \\ &= \phi_0 + Af(Z)\cos 2\pi(\zeta/\theta - P(Z))\, e^{\mu\zeta},\end{aligned} \tag{19}$$

where $$\zeta = L/D - X, \quad f(Z) = (g^2(Z) + h^2(Z))^{\frac{1}{2}},$$

and $P(Z)$ is a phase angle, which is a function of Z.

The variation of the wavelength (θ) with Re, and the exponential decay μ in equation (19) are plotted in figures 6 and 7. As Re increases, θ decreases rapidly,

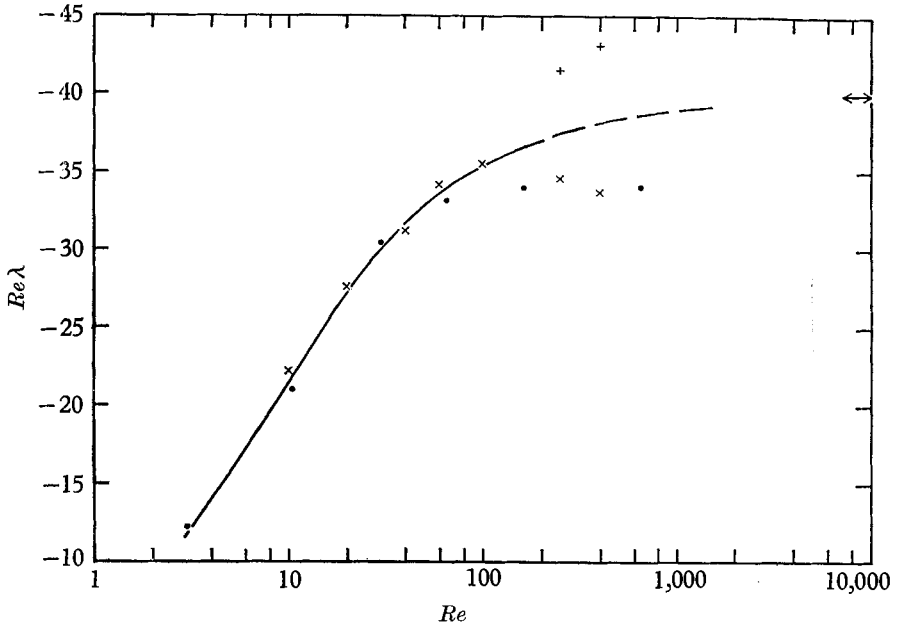

FIGURE 5. The upwind exponential decay. ×, Second-order relation solutions; +, third-order relaxation solutions; ●, eigensolution (15); ↔, $Re = \infty$.

rises to a slight maximum at about Reynolds number 200, and then decreases slowly to its limiting value. $|Re\,\mu|$ increases rapidly with Re, also appears to pass through a slight maximum at Reynolds number 200, and then decreases slowly to the limiting value

$$Re\,\mu = -150. \tag{20}$$

The physical interpretation is that in the limit $Re \to \infty$, the wavelength of the oscillation (θ) of the perturbation tends to a constant, and the decay factor (μ) tends to zero. At all finite Reynolds numbers (except 0), therefore, the downwind perturbation is a damped oscillation, as foreseen by our physical argument.

4. The full solutions of the vorticity equation

The perturbation analysis, of course, cannot show the streamfield in actual basins. We have therefore obtained relaxation solutions of the complete vorticity equation for a series of Reynolds numbers (0–400). In all solutions, except one, the upwind and downwind solutions are examined separately. At low Reynolds numbers, they are parts of the solution in the whole basin, while at higher Reynolds numbers they are considered in independent half-basins.

The interior region of these solutions approximates to the regime asymptotic to ϕ_0 in which the eigenequation is valid. In this region, relaxation estimates of

the eigenparameters have been calculated and compared with the eigensolutions of the previous section. The constant A in equations (14) and (19) has also been estimated for both the upwind and downwind circulations. The one exception is a solution for a short basin at Reynolds number 400.

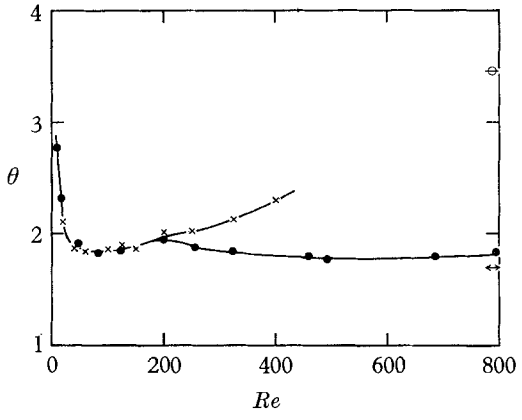

FIGURE 6. The downwind oscillation wavelength. ×, Relaxation solutions; ●, eigensolutions (15); ↔, $Re = \infty$; ⊖, $Re = \infty$ (special solution).

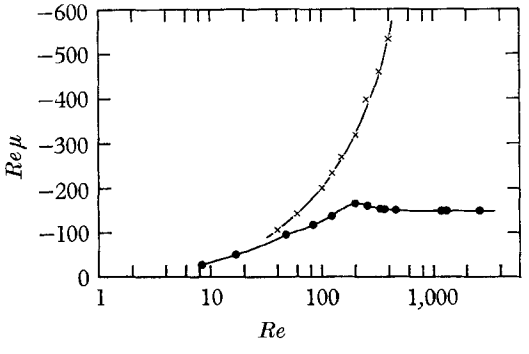

FIGURE 7. The downwind exponential decay. ×, Relaxation solution; ●, eigensolution (15).

(*a*) *The relaxation procedure*

Let us consider the solution of equation (7) on the network of the half-basin shown in figure 8, and assume that the half-basin is sufficiently long for the mid-basin solution to be applied as the interior boundary condition†

$$\phi)_{X=A} = \phi_0, \quad \left.\frac{\partial\phi}{\partial Z}\right)_{X=A} = 0,$$

where A is the length of the half-basin. The first step in obtaining the solution was to derive suitable finite-difference approximations to the equations of motion, and the boundary conditions. To this end, second- and third-order approximations were obtained, and applied to a variety of networks defined by

† The actual criterion was $|\phi(Z) - \phi_0(Z)|/\phi_0(Z) \lesssim 0{\cdot}5$ along any horizontal grid in the region $\frac{1}{2}A \leqslant X \leqslant A$. In the whole basin solutions, the boundary conditions of § 2 were used.

suitable choices of the X and Z grid intervals, h_X and h_Z respectively (cf. table 3). For example, for an interior point (P) with co-ordinates (j,k) in a network with equal grid intervals ($h_X = h_Z = h$), the stencil of the second-order finite-difference approximation to the equation of motion is

$$\frac{1}{h^4}\begin{bmatrix} & & 1 & & \\ & 2 & -8 & 2 & \\ 1 & -8 & 20 & -8 & 1 \\ & 2 & -8 & 2 & \\ & & 1 & & \end{bmatrix}\phi(j,k)$$

$$-\frac{Re}{h^4}\begin{bmatrix} & & & & & & -1 & & \\ & -1 & [1] & 1 & & -1 & 4 & -1 & \\ -1 & 4 & 0 & -4 & 1+ & [-1] & 0 & [1] & \\ & -1 & [-1] & 1 & & 1 & -4 & 1 & \\ & & & & & & 1 & & \end{bmatrix}\phi(j,k)+O(h^2) = 0,$$

where the coefficients in small brackets represent two-term finite-difference operators which multiply the remaining coefficients.

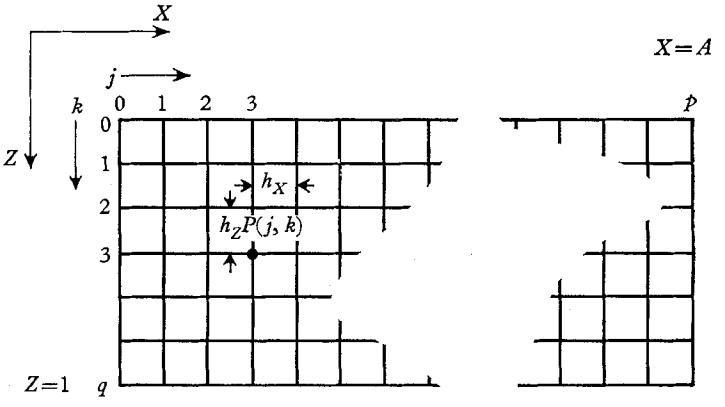

FIGURE 8. An upwind end network.

The set of finite-difference equations was then solved by various relaxation procedures, which have been fully described elsewhere (Bye 1962, 1965). The solutions had one dominant characteristic. As the Reynolds number increased, the horizontal resolution required changed: at the upwind end, it was sufficient to use large horizontal grid intervals ($h_X \gg h_Z$), but at the downwind end, especially near the wall, small horizontal grid intervals ($h_X \ll h_Z$) were essential. The large grid intervals at the upwind end solely decreased the number of network points required for the convergence and hence reduced the convergence time. Small grid intervals at the downwind end, however, were necessary to eliminate from the solution numerical oscillations which have no reality for the differential equation. Figure 9 illustrates two solutions at Reynolds number 200.

In the first solution on the network $h_X = h_Z = h = \frac{1}{6}$, oscillations of the ordinates ϕ with wavelength $2h$ are present, which are totally removed in the solution

on the finer network, $h_X = h_Z = h = \frac{1}{12}$. This behaviour appears to be consistent with two the limiting forms of the linearized vorticity equation observed in the eigensolutions. Another method of checking the accuracy of the numerical

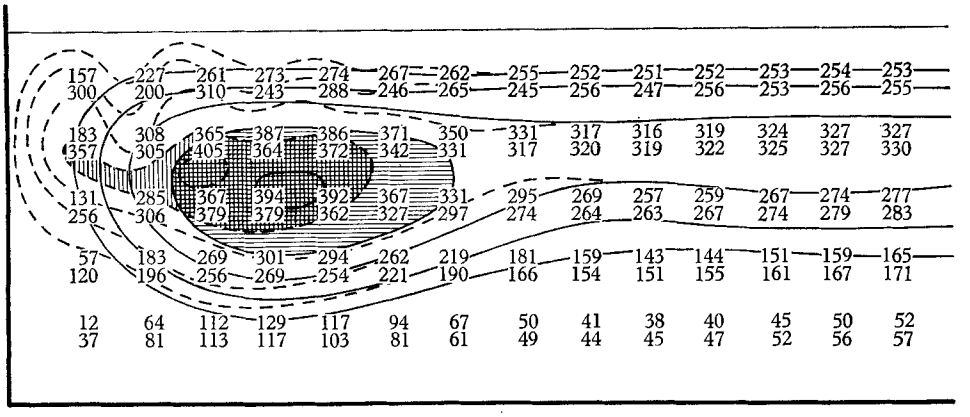

FIGURE 9. The Reynolds number 200 downwind solution. Top number: streamfunction for $h_Z = \frac{1}{12}$ network (solid streamlines), $\phi^1 > 350$ horizontal shading. Bottom number: streamfunction for $h_Z = \frac{1}{6}$ network (dashed streamlines), $\phi^1 > 350$ vertical shading.

solution was to apply a difference correction, by which the equations of motion are represented in the same network to a third-, instead of a second-order of approximation, i.e. with errors, $O(h^4)$. By this means, the amplitude of the numerical oscillation in the solution for a Reynolds number of 200 was reduced, and the solution at the upwind end somewhat improved, but the extra labour and computation involved was scarcely justified.

The groups of solutions are summarized in table 3, and a full discussion of probable errors in each group is given in the text.

The solutions are shown graphically in the unit (ϕ^1) used in the computer programmes namely, $\phi^1 = -8640\phi$. Asymptotic to the mid-basin flow, the streamfunctions are expressed thus,

$$\left.\begin{aligned} \text{upwind:} \quad & \phi = \frac{-\phi_0^1(Z)}{8640} + Af(Z)\, e^{\lambda X}, \\ \text{downwind:} \quad & \phi = \frac{-\phi_0^1(Z)}{8640} + Af(Z) \cos 2\pi(\zeta/\theta - P(Z))\, e^{\mu\zeta}, \end{aligned}\right\} \tag{21}$$

which are the finite-difference equivalents of the solution of the linearized vorticity equations (14) and (19); $\phi_0^1(Z)$ being the numerical mid-basin solution. The eigenfunction, $f(Z)$, is normalized so that its maximum value is 1, and is written as a group of five magnitudes at the five levels, $Z = \frac{1}{6}, \frac{1}{3}, \frac{1}{2}, \frac{2}{3}, \frac{5}{6}$ respectively, which correspond to the points of the most commonly used grid (cf. table 3). Near the walls the solutions are not in general quantitatively represented, but special features are noted. Non-dimensional surface profiles ($\xi\rho g D/\tau_s$), computed from equation (6), have also been outlined.

(*b*) *The Re = 0 circulation*

For $Re = 0$, equation (7) reduces to the biharmonic equation

$$\nabla^4 \phi = 0. \tag{22}$$

The solution of equation (18) is symmetrical about the centre of the basin, and is shown for the downwind end in figure 10.

The parameters λ and f, calculated from the region asymptotic to the mid-basin flow are recorded in table 1. There is approximate agreement with the solution of equation (16). The surface slope (computed by equation (6)) increases towards the end wall, a wall stress minimum occurs just above $Z = \frac{1}{6}$.

Group	Reynolds-number range	End of basin	No. of solutions	Network: No. of grids p	Network: No. of grids q	Network: Grid intervals h_X	Network: Grid intervals h_Z	Approximate computer time to obtain solution (min)
1	0–40	Whole	4	56	6	$\frac{1}{6}$	$\frac{1}{6}$	60
2	60–100	Whole	2	109	6	$\frac{1}{6}$	$\frac{1}{6}$	100
3	250–400	Upwind	2	33	6	*	$\frac{1}{6}$	30
4	250–400†	Upwind	2	33	6	*	$\frac{1}{6}$	30
5	100–125	Downwind	2	18	6	$\frac{1}{6}$	$\frac{1}{6}$	20
6	150–200	Downwind	2	24	6	$\frac{1}{6}$	$\frac{1}{6}$	30
7	200†	Downwind	1	33	6	$\frac{1}{6}$	$\frac{1}{6}$	150
8	200–250	Downwind	2	33	12	$\frac{1}{12}$	$\frac{1}{12}$	200
9	250–400	Downwind	3	*	6	*	$\frac{1}{6}$	200
10	400	Whole	1	*	6	*	$\frac{1}{6}$	180

* Groups 3 and 4, $h_X = 1$ for Reynolds number 250; $h_X = 2$ for Reynolds number 400. Groups 9 and 10, h_X is variable, increasing from $\frac{1}{24}$ near the wall to $\frac{1}{6}$ in the interior (group 9), or $\frac{1}{6}$ at the upwind end (group 10).

† Difference correction solutions.

TABLE 3. The relaxation solutions

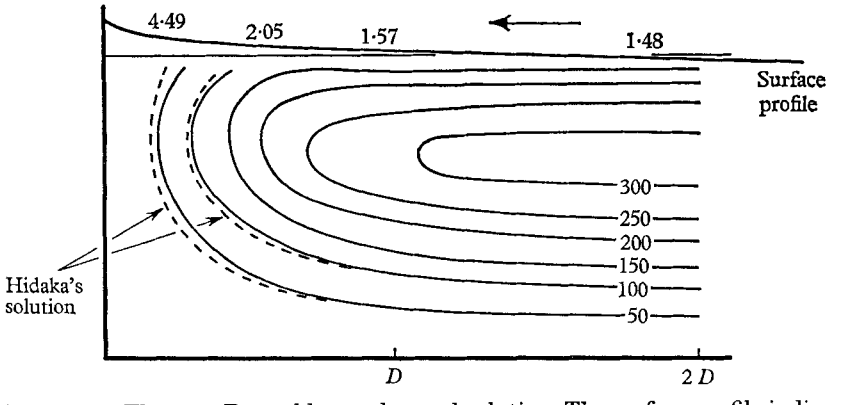

FIGURE 10. The zero-Reynolds-number end solution. The surface profile indices are coefficients of the non-dimensional slope $(\partial\xi/\partial x)/(\tau_s/\rho g D)$.

99 % of the mid-basin flow intensity, defined by

$$I = \int_0^D U_0^2 dz,$$

is attained within 2 depths of the wall.

Equation (22) has been solved previously with the same boundary conditions by Hidaka (1939). He determined the circulation in basins in which the length was two and four times the depth. The second of his solutions has end circulations which are virtually independent, and corresponds very closely with the present solution (figure 10). Our network ($h_Z = h_X = \frac{1}{6}$) therefore does not have appreciably different truncation errors from Hidaka's, although his network

$$(h_Z = h_X = \tfrac{1}{10})$$

is much finer.

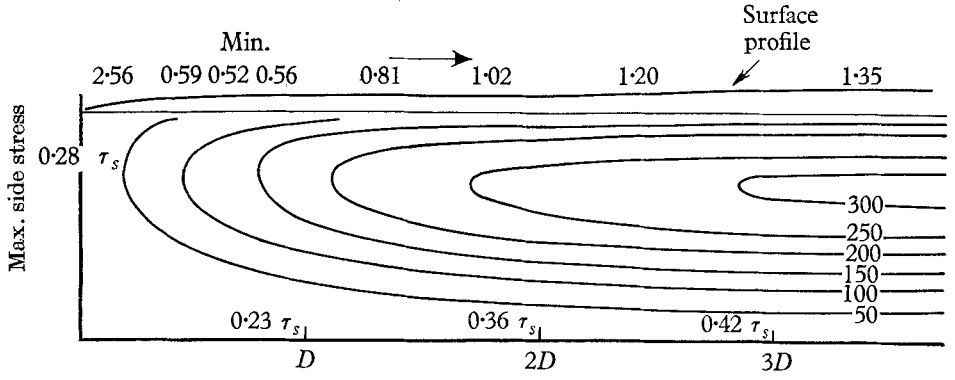

FIGURE 11. The Reynolds number 40 upwind solution. The surface profile indices are coefficients of the non-dimensional slope $(\partial\xi/\partial x)/(\tau_s/\rho g D)$.

(c) *The upwind end circulation*

The nine solutions obtained (two third-order, and seven second-order solutions) are listed in table 4. The solution for a Reynolds number of 40 is illustrated in figure 11. All the solutions are rather featureless. As the Reynolds number is increased the circulation becomes progressively slacker near the upwind wall. At Reynolds number 400, the flow does not come within 1 % of the mid-basin intensity until a distance of about 24 depths from the wall, compared with 2 depths for the viscous solution. In the asymptotic region the streamfunction increases exponentially to the mid-basin flow, as indicated by the eigensolutions. The parameters of the asymptotic circulation (21) are tabulated in table 4.

Notable features of the table are:

(i) At high Reynolds numbers (> 100) the coefficient A tends to a constant A_U. Slightly different estimates of A are given by the second- and third-order solutions, and its probable value is, $A_U = 0{\cdot}030 \pm 0{\cdot}002$.

(ii) The eigenfunction $f(Z)$ is similar at all Reynolds numbers.

(iii) The product $(Re\,\lambda)$ is plotted against Reynolds number in figure 5, for comparison with the eigensolution.

For Reynolds numbers > 50, the best fit from all the solutions satisfies equation (23),

$$\lambda = -B/(Re+C), \tag{23}$$

where $B = 40{\cdot}0 \pm 0{\cdot}05$, and $C = 9{\cdot}5 \pm 1{\cdot}0$. At high Reynolds numbers, the second- and third-order relaxation estimates appear to straddle the limiting eigenvalue, $Re\,\lambda$.

Reynolds number	A	λ	$f(Z)$				
			$Z \to 0{\cdot}167$	0·333	0·5	0·667	0·833
10	0·050	−2·22	0·65	1	0·95	0·63	0·23
20	0·034	−1·38	0·640	1	0·976	0·660	0·238
40	0·030	−0·78	0·646	1	0·973	0·667	0·246
60	0·031	−0·57	0·65	1	0·96	0·64	0·25
100	0·031	−0·335	0·67	1	1	0·64	0·26
250	0·031	−0·138	0·655	1	0·968	0·655	0·244
400	0·031	−0·084	0·655	1	0·968	0·655	0·244
250†	0·029	−0·166	0·65	1	0·96	0·62	0·19
400†	0·029	−0·108	0·65	1	0·96	0·62	0·19

† Difference correction solutions.

TABLE 4. The upwind parameters

In summary, the best numerical solution for the asymptotic upwind circulation at high Reynolds numbers ($Re > 250$) is

$$\left.\begin{aligned} \phi &= \phi_0 + A_U f_U(Z)\, e^{\lambda X}, \\ \text{where} \qquad A_U &= 0{\cdot}030 \pm 0{\cdot}002, \quad \lambda = (-40{\cdot}0 \pm 0{\cdot}05)/Re, \\ f_U(Z) &= [0{\cdot}66, 1, 0{\cdot}96, 0{\cdot}63, 0{\cdot}19]. \end{aligned}\right\} \tag{24}$$

The distance (δ) at which the circulation attains 99 % of the mid-basin intensity is given approximately by

$$\delta = 0{\cdot}06 Re\, D. \tag{25}$$

The surface slope has a minimum (cf. figure 11) near the wall, and then rises to its mid-basin value.

(*d*) *The downwind end circulation*

Eleven second-order solutions, and one trial third-order solution were computed for the downwind end of the basin. The Reynolds numbers 40 and 400 solutions are shown in figure 12. The streamlines at this end of the basin are totally different from the upwind end; the main feature is a strong eddy circulation near the wall. As the Reynolds number is increased, the intensity of the circulation increases until at Reynolds numbers a little greater than 400, the eddy is strong enough to induce reversed flow in its lee, as a weak wall eddy of opposite circulation to the main flow (figure 12). When the solution is examined in detail, these eddies are found to be the most pronounced part of a damped oscillatory disturbance to the mid-basin flow which begins asymptotically at large distances, and increases exponentially in amplitude as the wall is approached. Stagnation points occur in the liquid at the nodes of the disturbance.

For the same Reynolds number, the distance from the wall at which the flow very nearly attains the mid-basin regime is less at the downwind end of the basin, than at the upwind end. This picture is entirely consistent with the downwind eigensolution.

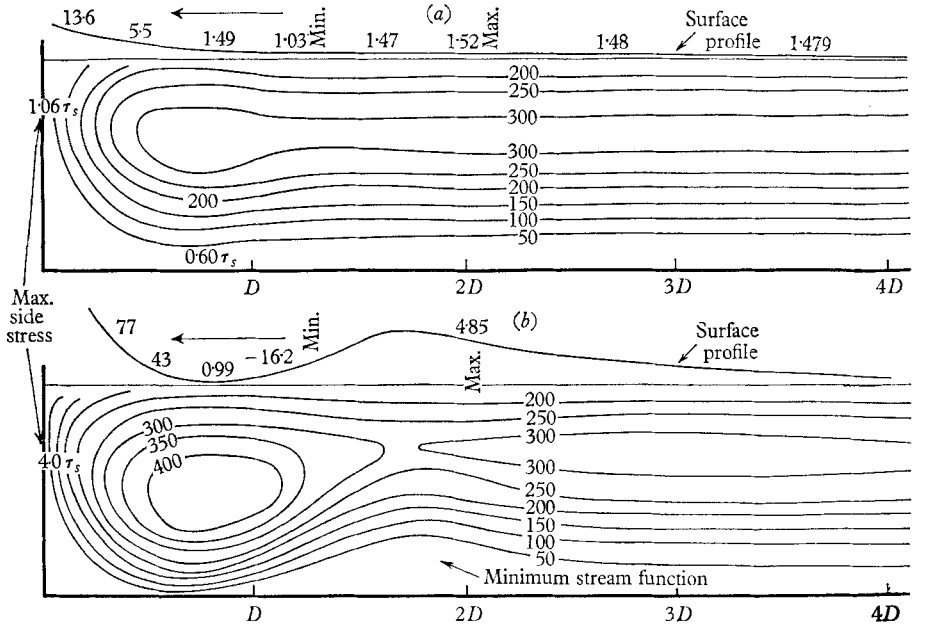

FIGURE 12. The Reynolds numbers (*a*) 40, and (*b*) 400, downwind solutions. The surface profile indices are coefficients of the non-dimensional slope $(\partial\xi/\partial x)/(\tau_s/\rho g D)$.

Reynolds number	A	θ	μ	P_0	$f(Z)$ $Z\rightarrow$ 0·167	0·333	0·5	0·667	0·833
10	.	.	·	.	0·13	0·72	1	0·92	0·58
20	.	2·10	.	0·50	0·36	0·80	1	0·96	0·54
40	−0·039	1·87	−2·66	0·515	0·296	0·687	1	0·921	0·445
60	−0·040	1·84	−2·40	0·48	0·24	0·64	1	0·93	0·52
100	−0·036	1·86	−2·02	0·46	0·18	0·56	1	0·99	0·56
125	−0·037	1·90	−1·89	0·38	0·17	0·54	1	0·99	0·58
150	−0·035	1·86	−1·80	0·38	0·21	0·53	1	0·99	0·60
200	−0·035	2·02	−1·60	0·36	0·20	0·52	1	0·96	0·60
250	−0·073	2·02	−1·59	0·44	0·21	0·55	1	0·95	0·60
325	−0·073	2·13	−1·42	0·44	0·20	0·53	1	0·94	0·61
400	−0·087	2·30	−1·39	0·44	0·18	0·48	0·98	1	0·61
200‡	−0·065	1·97	−1·82	0·46	0·19	0·52	0·90	1	0·57
250‡	−0·067	2·03	−1·70	0·46	0·18	0·51	0·85	1	0·52
200†	−0·050	2·06	−1·67	0·40	0·18	0·58	0·99	1	0·59

† Difference correction solution.
‡ $h = \frac{1}{12}$ network solutions.

TABLE 5. The downwind parameters

The parameters of equation (21) which best fit the solutions are summarized in table 5.

The notable features of the downwind asymptotic solutions are as follows.

(i) The coefficient A is approximately represented over the range of Reynolds numbers 0–400 by the relation

$$A = A_0 Re^{\gamma},$$

where $A_0 = -0{\cdot}010 \pm 0{\cdot}002$, and $\gamma = 0{\cdot}35 \pm 0{\cdot}02$. The log-log graph for this relation is plotted in figure 13.

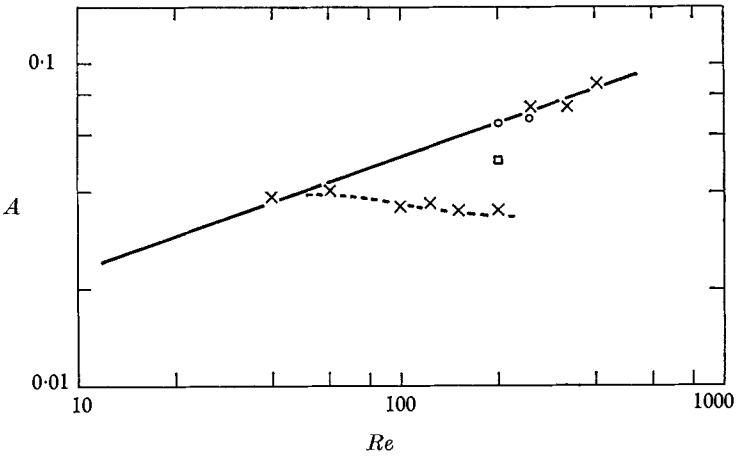

FIGURE 13. The downwind coefficient, A. ×, second-order relaxation solutions ($h_Z = \frac{1}{6}$); ○, second-order relaxation solutions ($h_Z = \frac{1}{12}$); □, third-order relaxation solutions ($h_Z = \frac{1}{6}$).

The behaviour of A at this end of the basin is completely different from the upwind end. At the upwind end, it is positive, and tends to a constant at high Reynolds numbers. At this end, it is negative (increased circulation in the final eddy), and increases to give significant oscillations at relatively low Reynolds numbers. Agreement is good between estimates of A from the $h_Z = \frac{1}{6}$ and $h_Z = \frac{1}{12}$ networks, but the solutions having the grid oscillation, discussed in §4*a*, give low values.

(ii) The eigenfunction $f(Z)$ is again similar at all Reynolds numbers. It does not, however, reach a limiting form until a Reynolds number higher than that for the upwind end. This is illustrated in figure 4, where the Reynolds number 40 and 400 eigenfunctions from the relaxation solutions have been plotted.

(iii) The exponential decay factor $|\mu|$ decreases, and the wavelength (θ) decreases and then increases slowly, as the Reynolds number increases.

Physically, this means that at small Reynolds numbers, the only important oscillation is the end eddy, but as the Reynolds number increases, the oscillations further from the wall become more pronounced.

The relaxation solution and the eigensolutions are in general agreement. However, figures 6 and 7 indicate that above Reynolds number 200, there are some rather significant differences in the behaviour of $Re\,\mu$ and θ as functions of

Re, for the two types of solutions. The cause of these differences is discussed in an appendix.

The conclusion of the discussion is that figure 12(*b*) probably shows oscillations with wavelength about 20% too high, and with a too rapid decay of the eddy chain away from the wall, i.e. the effect of the wall at the downwind end at high Reynolds numbers extends further than the relaxation solutions indicate—but not as far as at the upwind end.

(iv) The phase angle (P_0) for the centre mesh decreases only slightly as the Reynolds number is increased. This implies that as the wavelength is approximately constant, the centre of the wall eddy is about the same distance from the wall over the whole range of Reynolds numbers.

The variation in phase angle with depth is small in all the solutions ($\lesssim 10°$ at Reynolds number 40, and $\lesssim 30°$ at Reynolds number 325) and is such that the maximum of the oscillation is slightly nearer to the wall for the upper, than for the return flow. This behaviour is consistent with the solution of the linearized vorticity equation which predicts a constant phase angle at Reynolds numbers 0 and ∞ and a variation intermediately.

In summary, the best numerical estimate for the asymptotic solution, at high Reynolds numbers, at the downwind end of the basin, is

$$\left.\begin{aligned} \phi &= \phi_0 + A_D f_D(Z) \cos 2\pi\,((\zeta/\theta) - P_0)\, e^{\mu\zeta}, \\ \text{where} \qquad A_D &= (-0{\cdot}010 \pm 0{\cdot}002)\, Re^{0{\cdot}35 \pm 0{\cdot}02}\ (Re, 0\text{–}400), \\ \mu &= (-150 \pm 50)/Re, \quad \theta = 1{\cdot}70 \pm 0{\cdot}05, \\ P_0 &= 0{\cdot}40 \pm 0{\cdot}05, \quad f_D(Z) = [0{\cdot}22,\ 0{\cdot}70,\ 1,\ 0{\cdot}79,\ 0{\cdot}46]. \end{aligned}\right\} \tag{26}$$

Near the wall, the form of the solution is distorted from the asymptotic solution due to the finite amplitude of the oscillation. The distortion, however, even for Reynolds number 400 is not great, the non-linear interaction between the oscillatory perturbation, and the parent flow tending always to accentuate the oscillation.

A feature of the high Reynolds number solutions is the symmetry of the end eddy. For the solution for a Reynolds number of 400 the maximum surface, return and vertical currents are nearly equal. Associated with the return and vertical currents are wall boundary layers of thickness about $\frac{1}{10}$ the depth of the basin.

The surface slope, again computed from equation (6), is also oscillatory, with very large values near the wall, and a negative gradient upstream of the end eddy.

(*e*) *The hydrodynamic stability of the circulation*

Although we have only considered steady-state circulations, the Reynolds number at which instability is theoretically possible can be predicted, since Rayleigh's theorem I, states that a sufficient condition for instability is that the velocity profile should possess a point of inflexion. The Reynolds number at which such a point of inflexion is first realized is that at which reversed flow occurs. At Reynolds number 400, this condition has nearly been reached in the

lee of the wall eddy (figure 12). If we extrapolate, it is found that, at $Z = \frac{1}{6}$, ϕ is first negative (which implies reversed flow) at about Reynolds number 500.

As an approximation of the instability Reynolds number, this estimate is subject to two kinds of error; (i) the truncation errors of the solution, which have been discussed above and (ii), the fact that, even given a precise numerical solution, it is unlikely that ϕ will first become negative exactly at a grid point.

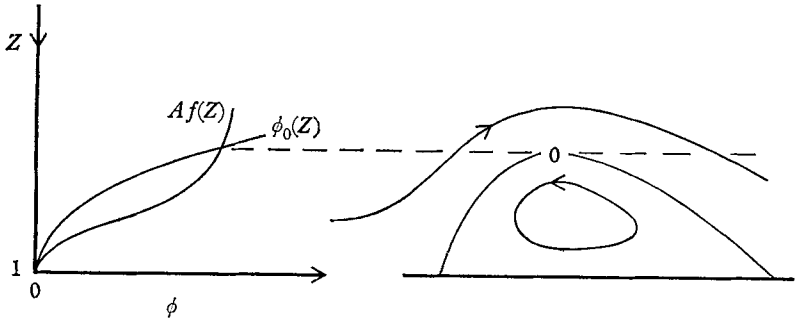

FIGURE 14. The reversed eddy.

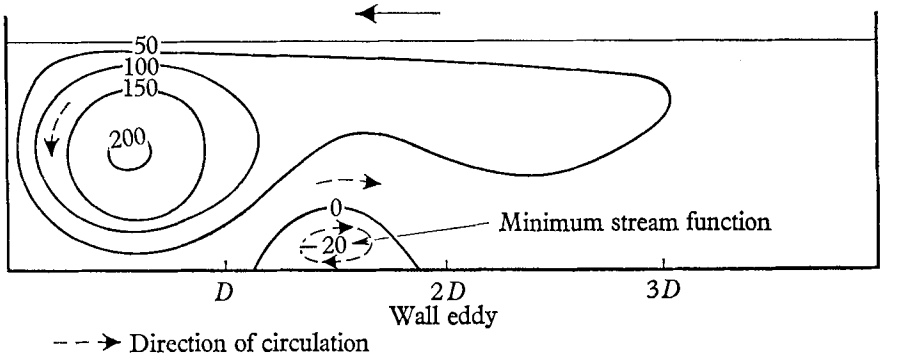

FIGURE 15. The short basin Reynolds number 400 solution.

On such considerations, we assign the error limit, ± 100, so that the true instability Reynolds number (Re_C) of an infinitely long basin lies in the range $Re_C = 400$ to 600. From the shape of the mid-basin streamfunction $\phi_0(Z)$, and the eigenfunction $f(Z)$, the form of the reversed eddy may be interpolated (figure 14).

The important feature is that $\phi_0(Z)$ is concave, while except very near the wall $f(Z)$ is convex. This gives rise, with the quasi-sinusoidal oscillation of amplitude, to the asymmetrical eddy shown. As the Reynolds number increases, $Af(Z)$ increases, and the eddy develops from the wall. For a short basin ($L = 4D$) at Reynolds number 400, such an eddy is actually observed (figure 15).

This solution was obtained to study the interaction of the end circulations. The main feature is the overall reduction in circulation intensity, and apparently a slightly decreased instability Reynolds number,

$$Re_C \approx 350.$$

These computed transitions are in order-of-magnitude agreement with wind-tunnel experiments by Keulegan. In a basin with an essentially vertical end wall, he observed a transition from laminar to turbulent flow in the range of Reynolds numbers 400–1000, and described the transition as follows: 'The passage from one type of flow to the other type does not show the steep and sudden transition ordinarily seen in fluid motion phenomena.' The significance of this remark is that the instability of closed-basin flow occurs through a secondary circulation, rather than directly from the parallel mid-basin flow. Such a mechanism ensures that the transition to turbulence occurs at a much lower Reynolds number than in the parallel flow cases, which are those 'ordinarily seen', and is consequently of a much less violent nature.

5. Discussion

The motive of this work has been to obtain bounded solutions of the equations of motion. We have studied the response to an applied surface stress of a liquid of uniform density enclosed in a Cartesian basin. The solutions reveal totally different interactions of the viscous and inertial terms at either end of the basin.

We shall discuss our results in two ways. First, let us contrast closed-basin flow with the more familiar pipe flow. Our mid-basin solution (ϕ_0) corresponds to Poiseuille flow. The behaviour at the upwind end is analogous to the development of the flow in the inlet of a pipe for the region in which the two wall boundary layers have merged (Schlichting 1962, pp. 168–171).

The behaviour at the downwind end, however, which is of special interest, has no direct *steady-state* analogy in pipe flow. The equivalent limiting process leads to the inviscid Orr–Sommerfeld equation, the solution of which is a travelling wave. This is because Poiseuille flow does *not* have an interior zero velocity point. Thus a singular solution can only be obtained with a travelling wave. In our case, the mid-basin velocity,

$$\phi_0'(Z) = 0 \quad \text{at} \quad Z = \tfrac{1}{3},$$

so that a travelling wave is not essential.

Now let us presume that a steady-state solution may exist at any Reynolds number and examine its properties for the range of Reynolds numbers ordinarily encountered in nature, say $Re \approx 10^7 - 10^{10}$. At these high Reynolds numbers the exponential decay factors in both the upwind and downwind solutions are very small. Hence the variation in the form of the solution along the basin is small. Further, the length of basin to attain the mid-basin flow is enormous, of order of magnitude, 10^6 to $10^9\, D$ (cf. equation 25), far greater than any naturally occurring basin. Therefore, in practice, the end circulations would always interpenetrate, and the mid-basin flow would never even be approached (figure 15 is an elementary example of this type of solution).

We may call such solutions almost fully developed 'steady-state turbulence' solutions. They are very close to the limiting, infinite Reynolds numbers (or basin convection) solutions, in which the exponential decay factors of equations (24) and (26) are exactly zero. At infinite Reynolds numbers, the effect of the end walls would be 'felt' uniformly throughout the basin, or in other words, the

mid-basin (or basin conduction) solution would only be attained at an infinite distance from the walls. The relation between this hypothetical 'steady-state turbulence' and natural turbulence is an intriguing question. The answer to which of course, lies in making the above qualitative reasoning quantitative; how can even steady-state solutions be obtained at high Reynolds numbers?

As we pointed out in §4*a*, there are difficulties in extending the numerical solutions by the present techniques. Analytical techniques, having failed to readily yield results at low Reynolds numbers, also, do not appear to be full of promise. In a further paper, therefore, we adopt another procedure, we change our boundary conditions, but nevertheless consider solutions of the vorticity equation which have the same essential character.

I thank the Director of the University of London Computer Unit for allocating the computer time on the Ferranti Mercury Computer, without which most of the investigation could not have been made, and also Mrs John Hays of the University of California who assisted in the later computations.

I am also grateful to the Department of Scientific and Industrial Research for providing the Research Studentship through which a major part of the work was made possible.

Many helpful comments by the referees, in particular the physical argument of §3*c*, are also acknowledged.

Appendix

The truncation errors in the downwind relaxation solutions

The cause of the differences between the eigensolution and the relaxation solutions is almost certainly the unfortunate fact that the relaxation networks have a grid point actually on the singular point, $Z = \frac{1}{3}$, of the inviscid limit (18) of the linearized vorticity equation. At this point $\phi_0'(Z) = 0$. The singularity is logarithmic, and has the form

$$f = 1 \pm 3\epsilon \ln \epsilon,$$

where $\epsilon = Z - \frac{1}{3}$ and as $\epsilon \to 0, f \to 1$, and f' and $f'' \to \infty$.

This circumstance gives rise to significant truncation errors as the inviscid behaviour dominates at large Reynolds numbers.

The above reasoning was checked by obtaining a special solution of equation (18) in which the truncation errors of the relaxation solutions were exactly reproduced, i.e. ϕ_0 was replaced by its finite-difference approximation ϕ_0^1. The wavelength from this eigensolution was significantly greater ($\theta = 3{\cdot}45D$ compared with $1{\cdot}70D$), indicating that the increase in θ (and also $|\mathrm{Re}\,\mu|$) at high Re in the relaxation solutions is almost certainly spurious (figures 6 and 7).

A comparison of the eigenfunction of this special solution with $f(Z)$, however, shows that the probable truncation errors of the relaxation eigenfunctions are small (cf. figure 4).

REFERENCES

BYE, J. A. T. 1962 Ph.D. Thesis, London University.
BYE, J. A. T. 1965 *Computer J.* **8**, 53–56.
BYE, J. A. T. 1966 *Computer J.* (submitted for publication).
HIDAKA, K. 1939 *Mem. Imp. Mar. Obs.* **7**, no. 1.
KEULEGAN, G. H. 1951 *J. Res. Nat. Bur. Standards* **46**, 358–381.
SCHLICHTING, H. 1962 *Boundary Layer Theory*. New York: McGraw-Hill.